High-Temperature Materials

SCIEPublish

Article

Simultaneous Fabrication of Ti–Si Alloy and CA–CA_2 Based Tailing Slag Cement via Aluminothermic Reduction of Ferrotitanium Slag

Xifei Zhang [1,2], Tu Long [1,2], Ding Chen [1,2,*], Huazhi Gu [1,2], Ao Huang [1,2], Lvping Fu [1,2], Yongshun Zou [1,2], Shenghao Li [1,2] and Xin Xiao [3]

[1] State Key Laboratory of Advanced Refractories, Wuhan University of Science and Technology, Wuhan 430081, China; 17302742681@163.com (X.Z.); 15618951629@163.com (T.L.); guhuazhi@wust.edu.cn (H.G.); huangao@wust.edu.cn (A.H.); fulvping@wust.edu.cn (L.F.); yongshun_zou@wust.edu.cn (Y.Z.); lishenghao@wust.edu.cn (S.L.)

[2] International Joint Laboratory on New Technologies of Refractories and Metallurgy, Wuhan University of Science and Technology, Wuhan 430081, China

[3] Ji'an Taihe Ecological and Environmental Monitoring Station, Ji'an 343700, China; X20170101441@163.com (X.X.)

* Corresponding author. E-mail: chending@wust.edu.cn (D.C.)

Received: 16 June 2026; Revised: 31 July 2026; Accepted: 20 August 2026; Available online: 7 September 2026

ABSTRACT: Al_2O_3–TiO_2–CaO-based ferrotitanium slag is a waste slag generated during ferrotitanium-alloy smelting. At present, the TiO_2 resource (about 15 wt.%) in ferrotitanium slag has not been effectively utilized. In this study, aluminothermic reduction was used to extract Ti and prepare a Ti–Si alloy, while the low-density Al_2O_3–CaO-based molten tailing slag floating on the Ti–Si melt was separated to fabricate CA–CA_2 tailing-slag cement. The TiO_2 content decreased from 14.42 wt.% in the ferrotitanium slag to 1.63 wt.% in the tailing slag. The Ti–Si alloy was mainly composed of Ti_5Si_3 and Ti_5Si_4. The mineral composition and hydration behavior of the CA–CA_2 tailing-slag cement were similar to those of commercial calcium aluminate cement Secar71. Under the adopted preparation and testing conditions, the mechanical strength of the tailing-slag cement paste reached approximately 85% of that of Secar71, indicating its potential as an alternative refractory binder. The co-production of Ti–Si alloy and CA–CA_2 tailing-slag cement provides a potential route for the value-added utilization of ferrotitanium slag.

Keywords: Ferrotitanium slag; Ti extraction; Aluminothermic reduction; Ti–Si alloy; Tailing slag cement

1. Introduction

Ferrotitanium slag is a byproduct of ferrotitanium alloy smelting by aluminothermic method [1–5]. The yield of ferrotitanium alloy and ferrotitanium slag is close to 1:1. It is a metallurgical solid waste with main compositions belonging to CaO–Al_2O_3–TiO_2–Ti_2O_3 high temperature phase system [6,7]. Furthermore, some high-temperature molten phases exist in the waste slag in a metastable state, which makes the phases

of the ferrotitanium slag complex. Massive accumulation of ferrotitanium slag not only pollutes the environment, but also causes waste of resources [8]. Therefore, it is urgent to make full use of ferrotitanium slag. Researchers found that ferrotitanium slag is an excellent refractory raw material, which has the advantages of high refractoriness, good slag corrosion resistance, and low thermal conductivity [9–12]. Zhang et al. [13] prepared Al_2O_3–TiO_2–CaO composites by replacing bauxite with ferrotitanium slag. It is concluded that with the increase of sintering temperature, $Ca((Al_{0.84}Ti_{0.16})_2)_6O_{19}$ in ferrotitanium slag was decomposed to $CaAl_{12}O_{19}$, and the components containing Ti were dissolved and formed free rutile and $CaTiO_3$. Li et al. [14] used ferrotitanium slag instead of corundum as raw material, and found that ferrotitanium slag refractory was prone to crack propagation in the oxidation environment above 1280 °C, which provided valuable suggestions for improving the application stability of recycled raw refractory products.

However, ferrotitanium slag is mainly used as a cheap, low-grade raw material to produce building materials, ceramics, and refractories at present [15–17]. The rich Ti resource (about 15 wt.% TiO_2 in ferrotitanium slag) could not be effectively applied.

Titanium silicides, particularly Ti_5Si_3, have been investigated as potential high-temperature materials because of their high melting point, relatively low density, and oxidation and creep resistance [18–23]. Ti–Si alloys may also serve as precursors or metallurgical intermediates for silicide-containing materials. However, the product obtained in this work is a multiphase Ti–Si alloy rather than a structural titanium alloy, and further refining and application-specific evaluation are required. Therefore, recovering Ti from ferrotitanium slag in the form of a Ti–Si alloy may provide a route for value-added resource utilization [24–27].

Further, Ti extraction from ferrotitanium slag produces a CaO–Al_2O_3-based tailing slag. This tailing slag can potentially be used to fabricate calcium aluminate cement similar to Secar71. Secar71 is a commonly used binder for refractory castables [28–31]. Its main mineral phases are $CaAl_2O_4$ (CA) and $CaAl_4O_7$ (CA_2) [32,33]. CA is the principal hydraulic phase and is mainly responsible for early strength development. Developing an alternative binder from tailing slag may improve the overall resource efficiency of the process.

In this article, the aluminothermic reaction was used to extract Ti from ferrotitanium slag. The Ti–Si alloy and CA–CA_2 based tailing slag cement were designed as target products to realize high value-added application of ferrotitanium slag.

2. Experimental Procedures

Ferrotitanium slag (1–0 mm), lime (3–0 mm), Al particles (2.5–0 mm), and SiO_2 powder (0.073–0.075 mm) were used as raw materials. Their chemical compositions are listed in Table 1. The raw-material ratio and target-product compositions were designed based on the chemical compositions and thermodynamic calculations.

The industrial trial used 3400 kg of ferrotitanium slag, 358.7 kg of Al particles, 225.4 kg of SiO_2 powder, and 1078.1 kg of lime, giving a total charge of 5062.2 kg. First, 1000 kg of the charge was placed in the bottom of an 800 kW electric arc furnace and heated by arc ignition until molten; the remaining charge was then added gradually using a bucket elevator and screw feeder. The total smelting time was 8 h. After smelting, the products were furnace-cooled to room temperature and manually recovered, yielding 284 kg of alloy and 4551 kg of tailing slag. The industrial operation was controlled by the recorded furnace power and processing time; a continuous melt-temperature history, numerical heating/cooling rates, and a separate isothermal holding stage were not recorded.

Table 1. The chemical compositions of raw materials for the aluminothermic method (wt.%).

Raw Materials	TiO_2	Al_2O_3	CaO	MgO	SiO_2	Fe_2O_3	Fe	Al	Si	Ca	Mn
Ferrotitanium slag	14.42	72.45	10.01	1.48	0.69	0.61					
Al							1.1	95.5	0.4	0.03	0.66
Lime			91.5		1.2						
SiO_2 powder					≥95						

The tailing slag was crushed and ground to pass a 0.044 mm sieve. The mechanical strength of the CA–CA_2-based tailing-slag cement was tested according to Chinese standard GB/T 201-2015. Paste specimens (140 mm × 25 mm × 25 mm) were prepared at a water-to-cement ratio of 0.3, kept in a cement-curing box until demoulding, and then cured in water for 1, 3, 7, and 28 d before testing. Particle-size distribution and specific surface area were not independently measured in the original industrial program; therefore, the comparison with Secar71 is treated as a preliminary performance comparison under the adopted preparation conditions.

Thermodynamic and slag-viscosity calculations were performed using FactSage software 8.1. Phase compositions were analyzed using an X'Pert Pro powder X-ray diffractometer (Philips, Eindhoven, The Netherlands) at 40 kV and 40 mA with a scan rate of $0.02°\cdot s^{-1}$, and the phases were identified using HighScore Plus 3.0e (3.0.5) and the ICDD database. Field-emission scanning electron microscopy (SEM, NovaNanoSem400, FEI Company, Hillsboro, OR, USA) was used to observe the microstructure, and elemental compositions were examined by energy-dispersive spectroscopy. Hydration heat was measured using a TAM Air isothermal calorimeter (TA Instruments, New Castle, DE, USA) at 20 °C with 15 g of powder and a water-to-cement ratio of 0.3.

3. Results and Discussion

3.1. Thermodynamic Analysis and Design of Aluminothermic Reduction

As shown in Table 1, ferrotitanium slag is mainly composed of Al_2O_3, CaO, and TiO_2, with small amounts of MgO, SiO_2, and Fe_2O_3. As indicated in Figure 1, the direct aluminothermic reduction of MgO and CaO is thermodynamically less favorable than that of TiO_2, SiO_2, and Fe_2O_3. Nevertheless, MgO and CaO may participate in the formation of slag phases containing $CaTiO_3$ and $MgAl_2O_4$, while the oxides of Ti, Si, and Fe may undergo competing aluminothermic reduction reactions.

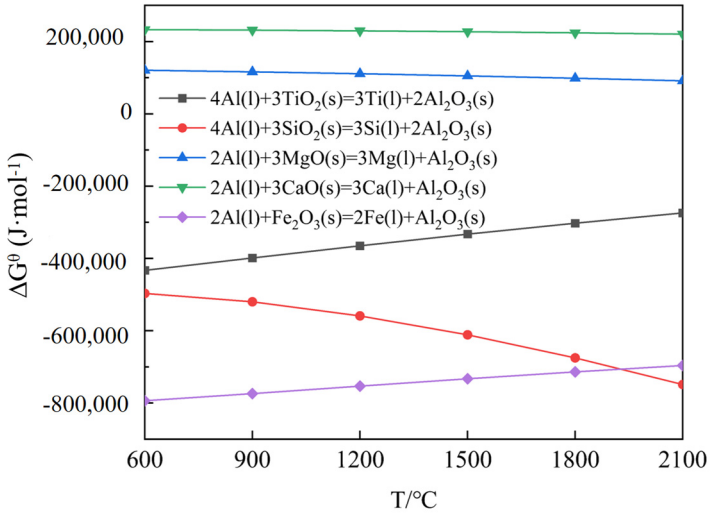

Figure 1. Standard Gibbs free energy changes of reactions between Al and different oxides in ferrotitanium slag.

Therefore, the extraction of Ti was designed by reference to the Fe–Si–Ti ternary phase diagram shown in Figure 2. The diagram was used only as a qualitative composition-design guide because the actual system also contained Al, O, Ca, and Mg. Ti_5Si_3 was selected as the target alloy phase because of its stability in the Ti-rich composition region and its high melting point. For the reduction of ferrotitanium slag, the charge was designed to convert TiO_2 toward Ti_5Si_3 formation. SiO_2 powder was added as a supplementary Si source and composition-adjusting reagent. The reaction is shown in Equation (1).

$$15TiO_2(s) + 32Al(l) + 9SiO_2(s) = 3Ti_5Si_3(s) + 16Al_2O_3(s)$$

$$\Delta G^{\theta} = -5{,}443{,}388.08 + 140.79T \quad (1)$$

After the reaction of Ti extraction, Ti–Si melt formed and sank to the bottom because of its high density. The CaO–Al_2O_3 based molten tailing slag floated upon the Ti–Si melt. Since Al was used as a reducing agent, the content of $A1_2O_3$ in the tailing slag was high, which resulted in high Al_2O_3 tailing slag with high viscosity and poor fluidity. It was difficult to separate the alloy melt from the tailing slag.

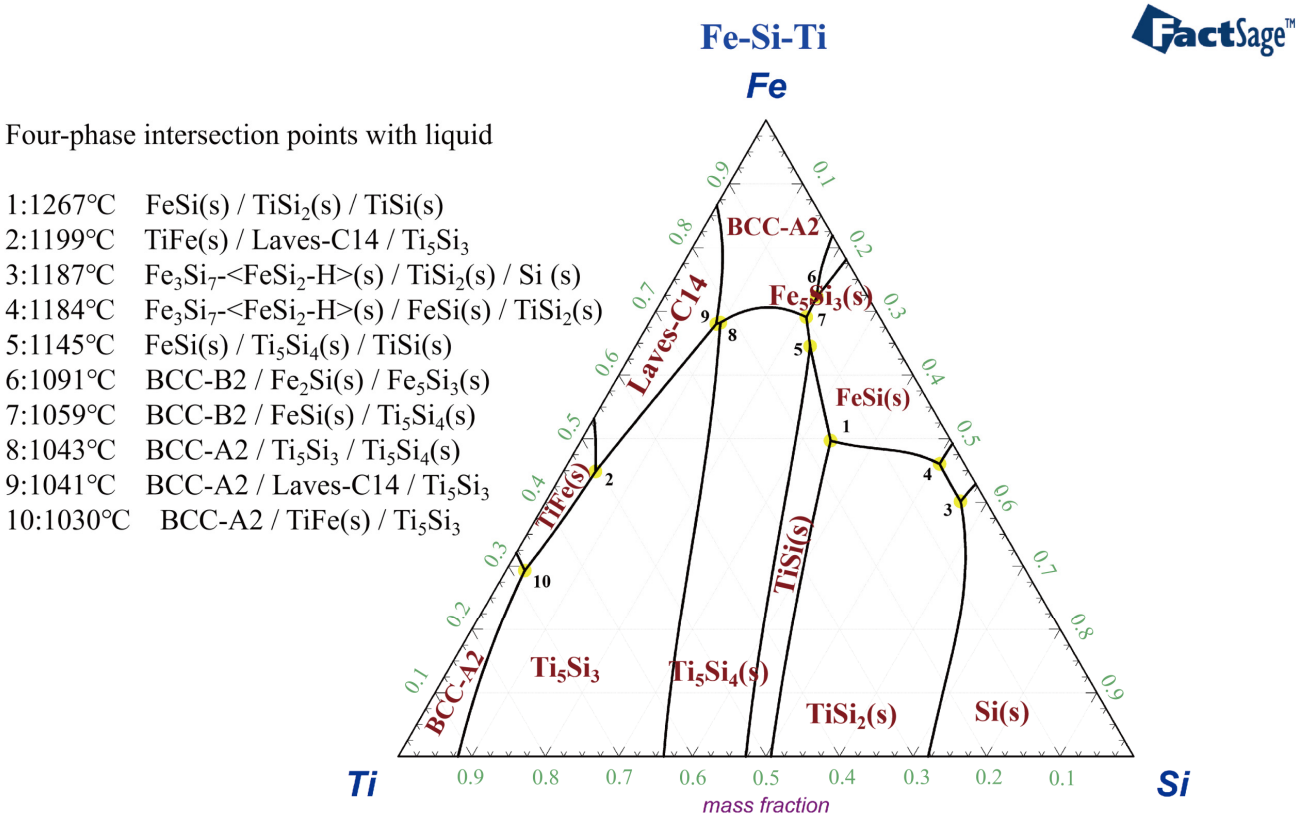

Figure 2. Fe–Si–Ti ternary phase diagram.

The viscosities of slags with different Al_2O_3/CaO ratios were calculated using the FactSage Viscosity module and are shown in Figure 3. Increasing the CaO content and temperature decreased the calculated viscosity. An Al_2O_3/CaO mass ratio in the range of 1–2 was therefore selected to improve slag fluidity. After cooling, the adjusted composition favored the formation of $CaAl_2O_4$ (CA) and $CaAl_4O_7$ (CA_2), similar to the principal phases of commercial calcium aluminate cement Secar71. Lime was added to adjust the nominal Al_2O_3/CaO mass ratio to 70/30.

$$CaO(s) + Al_2O_3(s) = CaAl_2O_4(s)$$

$$\Delta G^{\theta} = -24{,}042.13 - 19.04T \quad (2)$$

$$CaO(s) + 2Al_2O_3(s) = CaAl_4O_7(s)$$

$$\Delta G^{\theta} = -30{,}462.22 - 26.88T \quad (3)$$

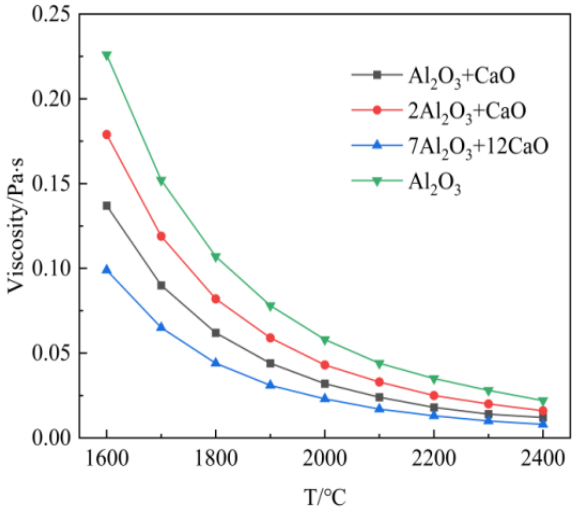

Figure 3. Calculated viscosity (Pa·s) of CaO–Al_2O_3-based slags with different Al_2O_3/CaO ratios.

The ferrotitanium slag was reduced by Al to extract Ti, and SiO_2 powder was used as a supplementary Si source and composition-adjusting reagent for titanium-silicide formation. Lime was added to the CaO–Al_2O_3-based molten tailing slag to reduce its viscosity and adjust its composition. Slag–the density difference promoted metal separation, improved slag fluidity, metallic-droplet coalescence, and gravitational settling. Ti–Si alloy and CA–CA_2-based tailing-slag cement were obtained after cooling.

In conclusion, Ti_5Si_3-containing Ti–Si alloy and CA–CA_2-based tailing-slag cement were designed as the target products for the value-added utilization of ferrotitanium slag. As shown in Figure 4, ferrotitanium slag, Al, SiO_2 powder, and lime were used to simultaneously fabricate Ti–Si alloy and CA–CA_2-based tailing-slag cement through aluminothermic reduction, slag–metal separation, and cooling crystallization.

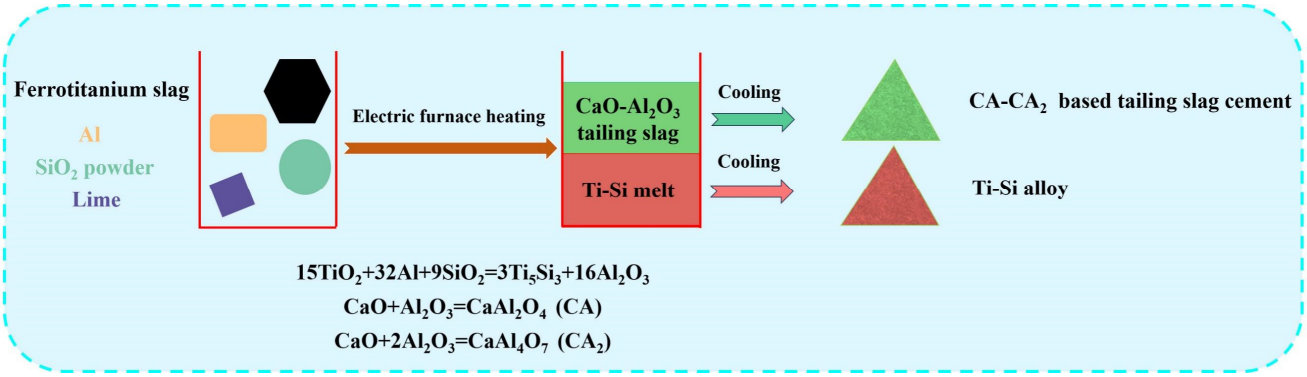

Figure 4. Schematic diagram of high value resource utilization of ferrotitanium slag.

3.2. Analysis of Smelting Products

3.2.1. Ti–Si Alloy

The XRD pattern of the Ti–Si alloy is shown in Figure 5. The main phases were Ti_5Si_3 and Ti_5Si_4, with a small amount of an Fe–Ti–Si-rich phase. Small amounts of Al_2O_3 and $MgAl_2O_4$ inclusions were also detected. Although the charge was designed according to the stoichiometry of Ti_5Si_3, local Ti/Si variations during reduction, metallic-droplet coalescence, and non-equilibrium solidification may have promoted the coexistence of Ti_5Si_3 and Ti_5Si_4. Therefore, the product is regarded as a multiphase Ti–Si alloy rather than phase-pure Ti_5Si_3.

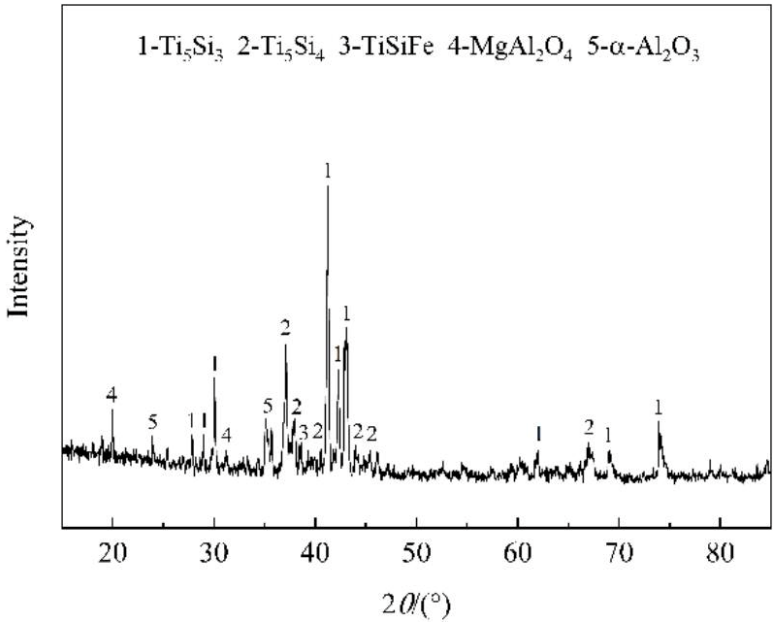

Figure 5. XRD pattern of alloy.

The microstructure of the Ti–Si alloy is shown in Figure 6, and the EDS results are listed in Table 2. The alloy was relatively compact, with few pores and cracks. An Al_2O_3-rich inclusion was observed at point 1, and an Mg–Al–O-rich inclusion was observed at point 5, consistent with the Al_2O_3 and $MgAl_2O_4$ phases identified by XRD. A Ti-rich region was observed at point 2, while points 3, 6, and 7 were mixed regions mainly containing Ti, Si, Al, and Fe.

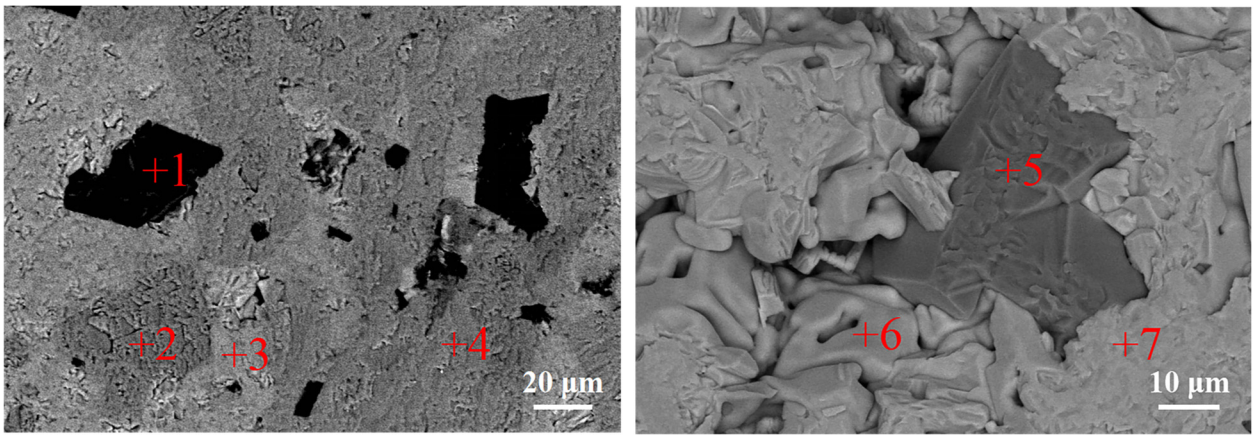

Figure 6. SEM images of Ti–Si alloy.

Table 2. Chemical composition of each point in Figure 6.

Point	Al	Ti	Si	Fe	O	Mg	Mn
1	43.71	—	—	—	54.03	2.26	—
2	—	100	—	—	—	—	—
3	24.84	27.58	25.79	21.79	—	—	—
4	—	81.18	18.82	—	—	—	—
5	43.26	—	—	—	37.56	19.18	—
6	2.46	67.87	26.03	3.64	—	—	—
7	9.81	37.39	35.84	15.52	—	—	1.44

The chemical composition of the Ti–Si alloy is shown in Table 3. The main elements were Ti, Si, Al, and Fe, while the contents of S, P, and Cu were low. The relatively high C content may be related to the

graphite electrode. The bulk Al content may include Al dissolved in the alloy as well as Al-bearing oxide inclusions entrained during slag–metal separation.

Table 3. Chemical compositions of Ti–Si alloy (wt.%).

Ti	Si	Al	Fe	O	C	Mg	Cu	P	S
57.24	20.44	10.22	6.52	2.27	1.67	1.24	0.18	0.02	0.01

3.2.2. CA–CA_2 Based Tailing Slag

The XRD pattern of the tailing slag is shown in Figure 7. The main phases were CA_2 and CA. CA is the principal hydraulic phase, whereas CA_2 generally exhibits lower hydraulic reactivity at room temperature.

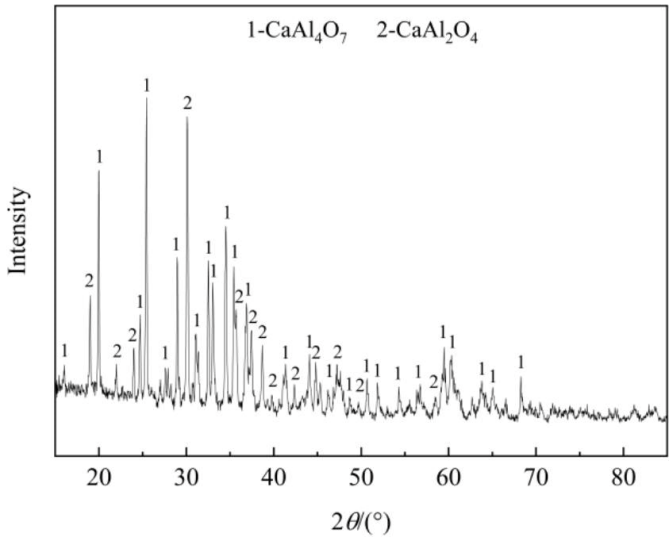

Figure 7. XRD pattern of tailing slag.

The microstructure of the tailing slag is shown in Figure 8. The slag was well crystallized. Because it was furnace-cooled, the relatively slow cooling process provided sufficient time for crystal nucleation and growth.

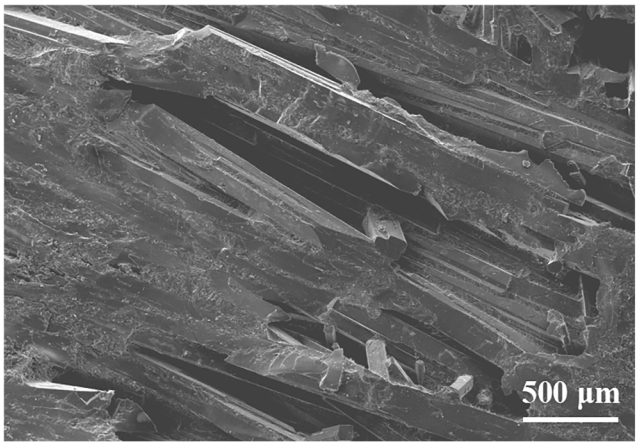

Figure 8. SEM image of tailing slag.

The chemical composition of the tailing slag is shown in Table 4. Al_2O_3 and CaO were the main components, together accounting for 94.70 wt.%, while the TiO_2 content was 1.63 wt.%. The TiO_2 concentration decreased from 14.42 wt.% in the feed slag to 1.63 wt.% in the tailing slag. Because the total slag mass changed due to Al oxidation and lime addition, this decrease in concentration is not reported as a true Ti recovery. The Al_2O_3/CaO mass ratio was 69.55/25.15, close to the design target of 70/30. After

aluminothermic reduction, a Ti–Si alloy mainly containing Ti_5Si_3 and Ti_5Si_4, and a CA–CA_2-rich tailing slag were obtained.

Table 4. Chemical composition of tailing slag (wt.%).

TiO_2	Al_2O_3	CaO	MgO	Fe_2O_3	SiO_2	K_2O	Na_2O
1.63	69.55	25.15	1.66	0.12	0.71	0.005	0.045

3.3. Hydration Performance Analysis of CA–CA_2 Based Tailing Slag

3.3.1. Hydration Heat Release of Tailing Slag

The hydration heat-flow and cumulative-heat curves of the tailing slag and Secar71 cement are shown in Figures 9 and 10. The first exothermic peak appeared 4 min after the addition of water. The initial heat-flow rate of the tailing slag (28.1 $mW \cdot g^{-1}$) was lower than that of Secar71 (38.5 $mW \cdot g^{-1}$), reflecting differences in wetting and dissolution. The second exothermic peak of the tailing slag occurred approximately 14 h later than that of Secar71. Because particle-size distribution and specific surface area were not independently measured, this delay cannot be attributed solely to phase composition or impurities. Most of the heat was released during this stage, and the cumulative hydration heat of the tailing slag (260.9 $J \cdot g^{-1}$) was close to that of Secar71 (255.9 $J \cdot g^{-1}$).

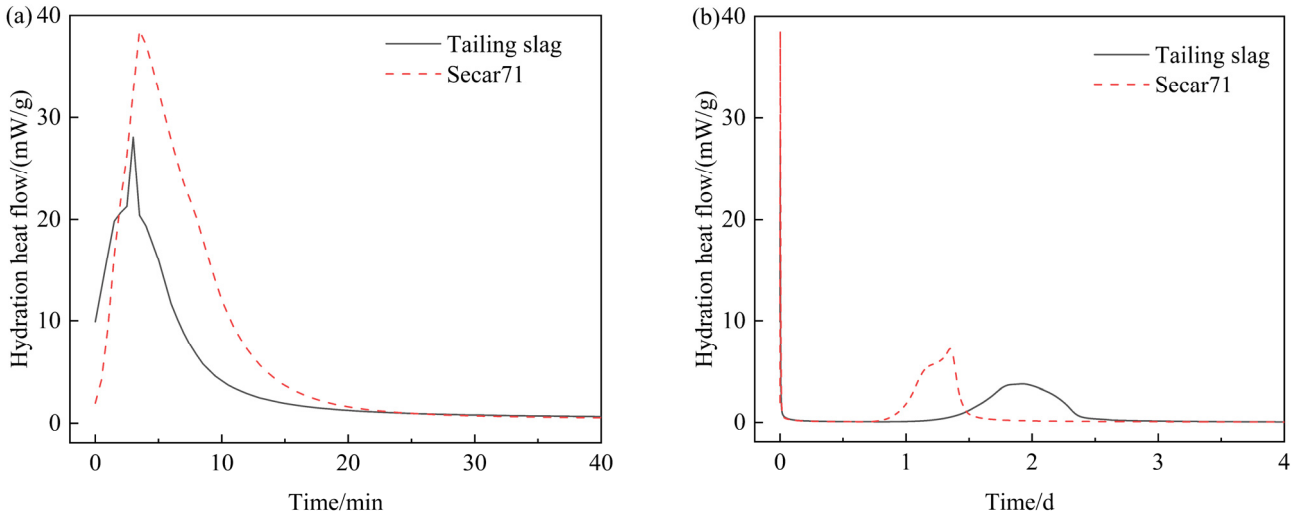

Figure 9. Hydration heat flow of tailing slag and Secar71 cement: (**a**) 0–40 min; (**b**) 0–4 d.

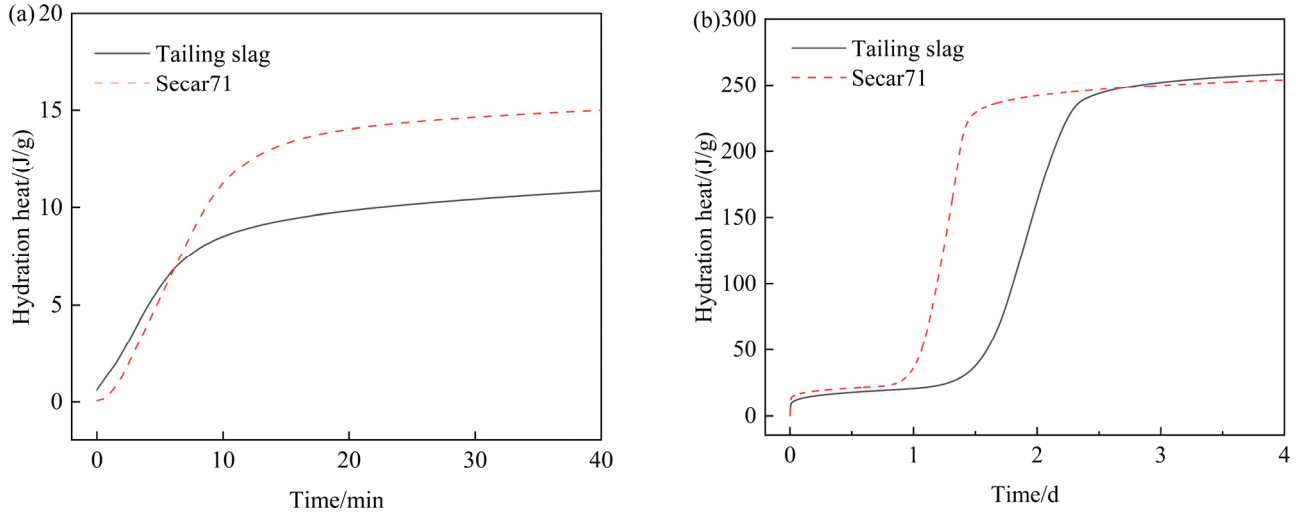

Figure 10. Hydration heat of tailing slag and Secar71 cement: (**a**) 0–40 min; (**b**) 0–4 d.

3.3.2. The Setting Time of Tailing Slag

The standard-consistency water demand, fluidity, and initial and final setting times of the tailing slag and Secar71 are listed in Table 5. Compared with Secar71, the tailing slag had a slightly higher standard-consistency water demand (28.1%), a slightly lower fluidity (12.8 cm), and longer initial (90 min) and final (179 min) setting times. The longer setting time may reflect the combined effects of powder fineness, phase composition, crystallinity, and minor Ti- and Mg- bearing phases; the present data do not distinguish their individual contributions. Overall, the hydration and hardening behavior were comparable to that of commercial calcium aluminate cement.

Table 5. The physical properties of tailing slag and Secar71 cement.

Raw Materials	Standard Consistency Water Consumption/%	Degree of Fluidity/cm	Setting Time/min	
			Initial Set	Final Set
Tailing slag	28.1	12.8	90	179
Secar 71	27.5	14.1	75	167

3.3.3. Hydration Strength of Tailing Slag

The cold modulus of rupture and cold crushing strength of the tailing-slag and Secar71 cement pastes at different curing ages are shown in Figure 11. The strength of the tailing-slag paste increased with curing age. Under the adopted preparation and testing conditions, the strength at different ages reached approximately 85% of that of Secar71. Because particle size, specific surface area, and quantitative phase fractions were not independently controlled, the strength difference cannot be assigned to a single cause and may reflect the combined effects of fineness, crystallinity, phase proportions, and minor Ti- and Mg-bearing phases. The comparison is descriptive, and complete specimen-level replicate records were not available for additional statistical reanalysis.

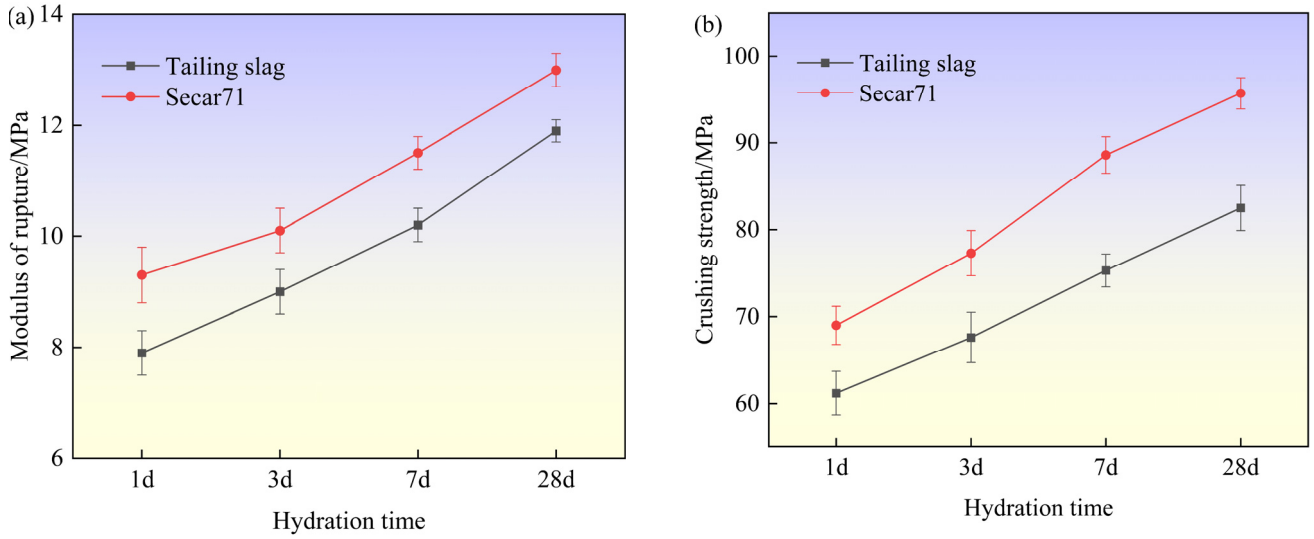

Figure 11. The mechanical performances of tailing slag and Secar71: (**a**) modulus of rupture of paste; (**b**) crushing strength of paste.

3.3.4. Analysis of Hydrate Phase of Tailing Slag

The XRD patterns of the hydrated tailing-slag samples are shown in Figure 12. At 1, 3, 7, and 28 d, the main detected phases were CA_2 and C_3AH_6, together with small amounts of CA and AH_3. With increasing hydration age, the CA_2 peak intensity decreased slightly, and the C_3AH_6 peak intensity increased. However, changes in individual diffraction peak intensities are insufficient to quantify CA_2 hydration, as preferred orientation and sample preparation may also affect peak intensities.

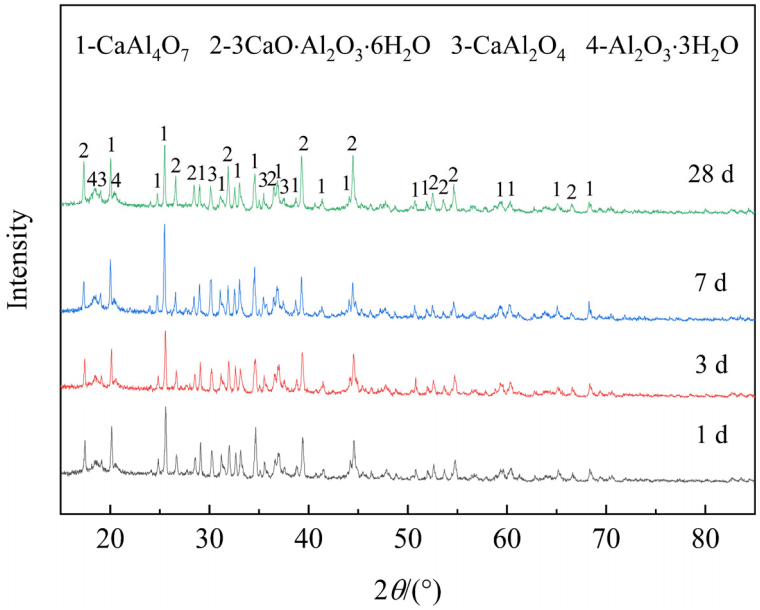

Figure 12. XRD patterns of hydration samples at different periods.

Compared with Figure 7, the lower intensities of the CA and CA_2 peaks are consistent with the progress of hydration, although the individual contributions of the two phases cannot be quantified from the present qualitative XRD data. Hydration involves surface hydroxylation and dissolution, producing Ca^{2+} and $Al(OH)_4^-$ species in the aqueous phase [34–36], as represented by Equation (5) [37].

$$CaAl_2O_4 + 4H_2O = Ca^{2+} + 2Al(OH)_4^- \quad (5)$$

The dissolved Ca^{2+} and $Al(OH)_4^-$ species subsequently precipitated as calcium aluminate hydrates. Because the earliest XRD measurement was conducted at 1 d, metastable CAH_{10} and C_2AH_8 may have formed at earlier ages and subsequently converted before the first measurement, or their contents may have been below the XRD detection limit.

3.3.5. Analysis of Hydration Morphology of Tailing Slag

The microstructure of tailing slag after hydration at different ages is shown in Figure 13. After 1 d hydration (Figure 13a,b), cubic C_3AH_6 appeared in the sample, but the amount was small, the crystal development was not perfect, and the distribution was relatively loose. No dense network structure formed, indicating that the degree of hydration of the tailing slag slurry was low after 1 d of hydration. After 3 days of hydration (Figure 13c,d), the C_3AH_6 crystal developed better. It appeared on the surface and in the voids, filling the pores of the tailings slag slurry and making the structure denser. Therefore, the mechanical strength of the tailing slag slurry after 3 days of hydration was larger. After 7 days of hydration (Figure 13e,f), a small amount of flake products (C_3AH_6) formed between the particles. After 28 days of hydration (Figure 13g,h), there were some plate-like and columnar hydration products (C_3AH_6). It was precisely because these needle-like, flake-like, and columnar hydrated crystalline products overlapped with the aluminum gel and were filled between the voids of the crystal particles that the degree of densification was improved, and the hydrated sample obtained high mechanical strength. As mentioned above, the amount and morphology of C_3AH_6 hydration products were significant to the strength.

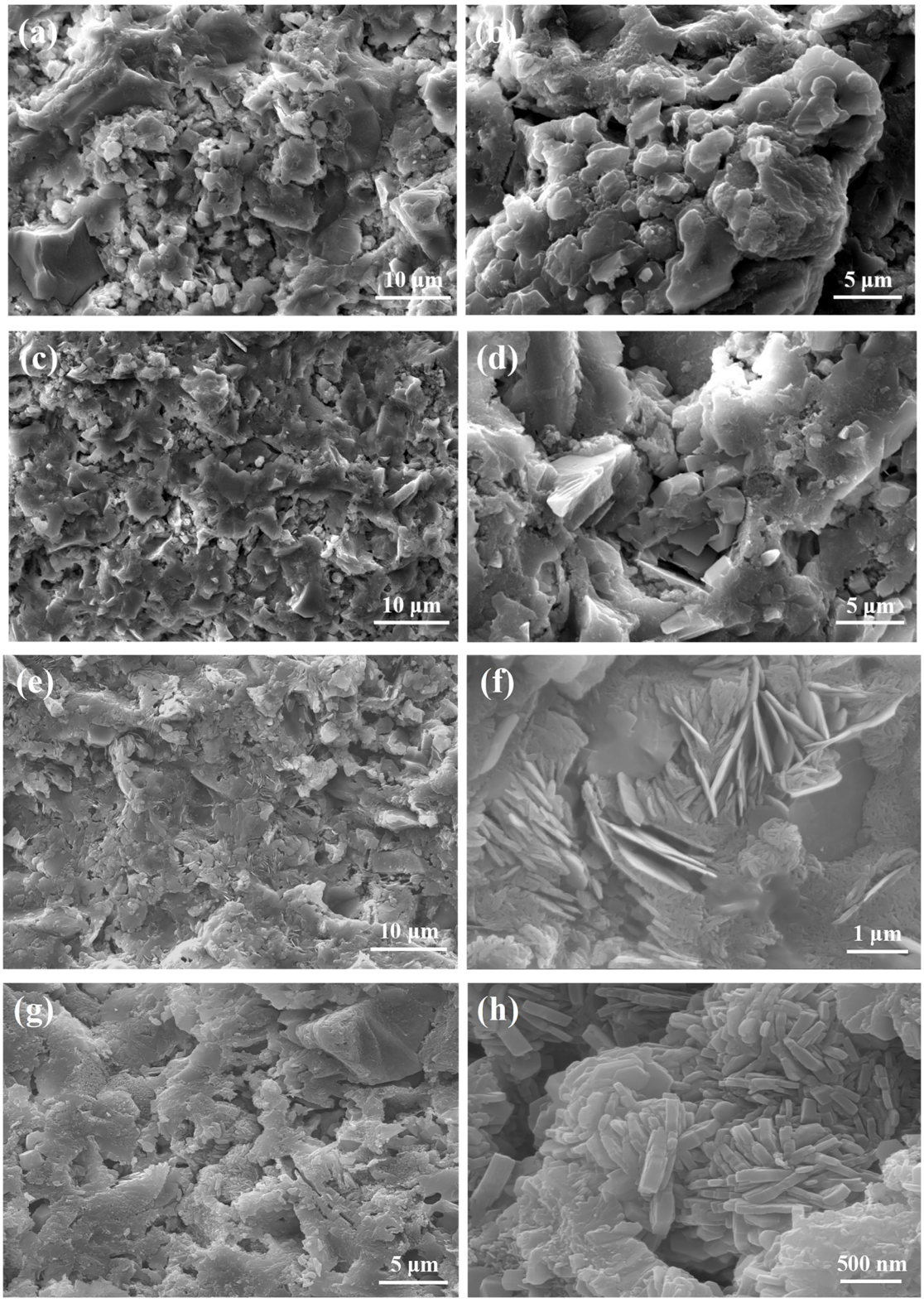

Figure 13. SEM images of tailing slag at different hydration periods: (**a**,**b**) 1 d; (**c**,**d**) 3 d; (**e**,**f**) 7 d; (**g**,**h**) 28 d.

Based on the recorded industrial charge, treatment of 1 t of ferrotitanium slag required approximately 105.5 kg Al, 66.3 kg SiO_2 powder, and 317.1 kg lime. The nominal furnace-energy input calculated from 800 kW for 8 h was approximately 1882 kWh per tonne of feed slag. These values show that reagent and energy consumption must be considered when evaluating scale-up. The present study demonstrates technical co-production feasibility; a full techno-economic and environmental assessment requires verified industrial electricity consumption, emissions, dust recovery, product refining, and market-quality data.

4. Conclusions

Aluminothermic reduction was used to extract Ti from ferrotitanium slag, and SiO_2 powder was used as a supplementary Si source and composition-adjusting reagent for Ti–Si melt formation. Lime was added to reduce the viscosity and adjust the composition of the CaO–Al_2O_3-based tailing slag. The alloy melt and molten slag were separated by the combined effects of density differences, slag fluidity, and gravitational settling, yielding Ti–Si alloy and CA–CA_2-based tailing-slag cement upon cooling.

(1) The main elements of the alloy were Ti, Si, and Al, and the contents of S, P, and Cu were low. The main phases were Ti_5Si_3 and Ti_5Si_4. The main mineral phases of the tailing slag were CA and CA_2, and the Al_2O_3 (69.55 wt.%) and CaO (25.15 wt.%) contents were close to those of Secar71 cement. The TiO_2 concentration decreased from 14.42 wt.% to 1.63 wt.%. This concentration change is not interpreted as a true Ti recovery without a closed elemental mass balance.

(2) The CA–CA_2-based tailing slag exhibited measurable hydraulic activity. Its hydration products and setting behavior were comparable to those of commercial calcium aluminate cement, Secar71. Under the adopted preparation and testing conditions, the mechanical strength at 1, 3, 7, and 28 d reached approximately 85% of that of Secar71. These results indicate the preliminary potential of the tailing slag as an alternative binder for refractory castables, subject to further validation under controlled fineness and actual service conditions.

Author Contributions

X.Z. analyzed the data, and wrote the original manuscript. H.G. built the model and related methodology. D.C. revised the manuscript. X.X. and L.F. analyzed the data and interpreted the results. T.L. and A.H. performed experiments and analyzed the experimental data. S.L. and Y.Z. provided the funds needed for the experiment.

Ethics Statement

Not applicable.

Informed Consent Statement

Not applicable.

Data Availability Statement

The data that support the findings of this study are available on request from the corresponding author.

Funding

This research was funded by [National Natural Science Foundation of China] grant number [52172023 and 52302027].

Declaration of Competing Interest

The authors declare that they have no known competing financial interests or personal relationships that could have appeared to influence the work reported in this paper.

References

1. Maeda M, Yahata T, Mitugi K, Ikeda T. Aluminothermic Reduction of Titanium Oxide. *Mater. Trans. JIM* **1993**, *34*, 599–603. DOI:10.2320/matertrans1989.34.599
2. Zhao K, Gao F. Mechanism and kinetic analysis of vacuum aluminothermic reduction for preparing TiAl intermetallics powder. *J. Alloys Compd.* **2021**, *855*, 157546. DOI:10.1016/j.jallcom.2020.157546

3. Wang Z, Zhang J, Liu Z, Wang G, Jiao K, Li K, et al. Production of ferrotitanium alloy from titania slag based on aluminothermic reduction. *J. Alloys Compd.* **2019**, *810*, 151969. DOI:10.1016/j.jallcom.2019.151969
4. Gao Z, Cheng G, Yang H, Xue X, Ri J. Preparation of Ferrotitanium Using Ilmenite with Different Reduction Degrees. *Metals* **2019**, *9*, 962. DOI:10.3390/met9090962
5. Gasik M, Dashevskii V, Bizhanov A. Metallurgy of Ferrotitanium. In *Ferroalloys: Theory and Practice*; Springer: Cham, Switzerland, 2020; pp. 201–218. DOI:10.1007/978-3-030-57502-1_11
6. Wu J, Zhang C, Xu X, Liu S, Cheng T, Ma S. Ceramic–molten salt composites (CPCMs) for high-temperature thermal energy storage: Improving sinterability and thermal stability by using solid wastes as skeletons. *Sol. Energy Mater. Sol. Cells* **2022**, *238*, 111651. DOI:10.1016/j.solmat.2022.111651
7. Wu J, Zhang C, Xu X, Liu X, Zhou S. Preparation and characterization of alumina/calcium-hexaluminate ceramic composites from ferrotitanium slag. *J. Eur. Ceram. Soc.* **2020**, *40*, 4265–4275. DOI:10.1016/j.jeurceramsoc.2020.05.004
8. Chen C, Liu H, Zhang Y, Gu G, Hu J. Micro-assessment of heavy metal immobilization within alkali-activated copper tailings-slag geopolymer. *Cem. Concr. Compos.* **2024**, *149*, 105510. DOI:10.1016/j.cemconcomp.2024.105510
9. Rechkalov D, Chernogorlov S, Abyzov V. Hydration of alumina cement containing ferrotitanium slag with polycarboxylate-ethers (PCE) additives. *AIP Conf. Proc.* **2016**, *1698*, 060013. DOI:10.1063/1.4937868
10. Ju MQ, Cai MF, Liang YH, Nie JH, Guo MZ. Application of calcium alumino-titanate to taphole clay. *J. Iron Steel Res. Int.* **2022**, *29*, 1089–1100. DOI:10.1007/s42243-021-00664-5
11. Chen J, Zhao H, Zhang H, Li Z, Zhang J. Effect of partial substitution of calcium alumino-titanate for bauxite on the microstructure and properties of bauxite-SiC composite refractories. *Ceram. Int.* **2018**, *44*, 2934–2940. DOI:10.1016/j.ceramint.2017.11.045
12. Rytvin VM, Perepelitsyn VA, Ponomarenko AA, Gil'varg SI. Titanium-Alumina Slag—Semifunctional Technogenic Resource of High-Alumina Composition. Part 2. Use of Ferrotitanium Slag for Producing Refractories in Metallurgy and Other Branches of Industry. *Refract. Ind. Ceram.* **2018**, *58*, 487–498. DOI:10.1007/s11148-018-0132-5
13. Zhang F, Zhang H, Zhao H, Xu J. Sintering properties and microstructure of Al_2O_3–TiO_2-CaO composite materials based on ferrotitanium slag. *Ceram. Int.* **2023**, *49*, 38256–38263. DOI:10.1016/j.ceramint.2023.09.157
14. Li Y, Zhao H, Ma J, Wang Y, Zhang H, Yu J, et al. Evaluation of remelting low-fluxing ferrotitanium slag as a potential refractory raw material: Thermal characteristics and stability. *Ceram. Int.* **2022**, *48*, 11192–11198. DOI:10.1016/j.ceramint.2021.12.339
15. Yang J, Wang Y, Peng J, Di Y. Reaction mechanism and kinetics of ferrotitanium preparation by aluminothermic reduction of $CaTiO_3$. *Mater. Today Commun.* **2022**, *30*, 102995. DOI:10.1016/j.mtcomm.2021.102995
16. Guo M, Liang Y, Cai M, Nie J, Ju M, Liu M, et al. Improved slag resistance of taphole clay due to in situ formation of TiCN from ferrotitanium slag. *Ceram. Int.* **2021**, *47*, 23630–23636. DOI:10.1016/j.ceramint.2021.05.082
17. Wu J, Zhang C, Xu X, Liu X, Zhou S, Wu C. Enhanced thermal shock resistance of ZrO_2-reinforced Al_2O_3–$CaAl_{12}O_{19}$ composites prepared from ferrotitanium slag: Crack propagation resistance mechanisms. *Ceram. Int.* **2021**, *47*, 14540–14550. DOI:10.1016/j.ceramint.2021.02.033
18. Gummadi J, Alanka S. A review on titanium and titanium alloys with other metals for biomedical applications prepared by powder metallurgy techniques. *Mater. Today Proc.* **2023**. DOI:10.1016/j.matpr.2023.04.387
19. Fattah-alhosseini A, Karbasi M, Bahramian H. A thorough investigation of the utilization of metal-organic framework (MOF) coated titanium dioxide in photocatalytic applications: A review. *Appl. Surf. Sci. Adv.* **2023**, *18*, 100504. DOI:10.1016/j.apsadv.2023.100504
20. Jesu Amalraj AJ, Wang SF. Synthesis of transition metal titanium oxide (MTiOx, M = Mn, Fe, Cu) and its application in furazolidone electrochemical sensor. *J. Ind. Eng. Chem.* **2022**, *111*, 356–368. DOI:10.1016/j.jiec.2022.04.018
21. Solodkyi I, Mosiichuk V, Kucher O, Krüger M. Synthesis and spark plasma sintering of Ti_5Si_3-Mo powders with core-shell structure. *Vacuum*, **2025**, 232, 113843. DOI: 10.1016/j.vacuum.2024.113843
22. Li Z, Du R, Fu L, Or SW, Gu H, Chen D, et al. Fabrication of $CaAl_{12}O_{19}$–$CaTiO_3$ composites and their potential usage for TiAl alloy smelting. *J. Am. Ceram. Soc.* **2023**, *106*, 7057–7068. DOI:10.1111/jace.19267
23. Qi X, Fu L, Du R, Gu H, Chen D, Yang S, et al. Properties of various CaO–Al_2O_3–TiO_2 refractories and their reaction behaviours in contact with Ti6Al4V melts. *J. Alloys Compd.* **2023**, *959*, 170599. DOI:10.1016/j.jallcom.2023.170599
24. Long T, Gu H, Zhang M, Huang A, Jiang Q, Fu L, et al. Effect of pretreated Al-Si alloy powder on the microstructure and properties of Al_2O_3–SiC–C castables for iron runner. *J. Alloys Compd.* **2024**, *986*, 174138. DOI:10.1016/j.jallcom.2024.174138
25. Li J, Wang S, Zhong J, Xin Y, Lv X, Zeng L, et al. Properties and microstructure development of alkali- activated coal bottom ash and titanium- extraction tailing slag binder. *Constr. Build. Mater.* **2023**, *403*, 133087. DOI:10.1016/j.conbuildmat.2023.133087

26. Song Y, Feng Q, Qiao H, Wei C. Study on mechanically activated ferrous extraction tailing of nickel slag as cementitious materials: Physical and chemical properties, mechanical properties and reaction mechanism. *Constr. Build. Mater.* **2024**, *422*, 135748. DOI:10.1016/j.conbuildmat.2024.135748
27. Zhang T, Dou Z, Zhang H, Zhang Z, Niu L, He J. Preparation of Titanium Ferrous Alloys with Low Oxygen Content Prepared by Reduction-SHS. In *3rd International Symposium on High-Temperature Metallurgical Processing*; John Wiley & Sons: Hoboken, NJ, USA, 2012; pp. 237–242. DOI:10.1002/9781118364987.ch29
28. Lei C, Xiao G, Ding D, Chen J, Zang Y. Microstructural evolution and properties enhancement of SiC refractory castables bonded with the special CNFs/calcium aluminate cement. *Ceram. Int.* **2023**, *49*, 25716–25727. DOI:10.1016/j.ceramint.2023.05.118
29. Lei C, Xiao G, Ding D, Shan J, Wang J, Zang Y, et al. One-step synthesis of core–shell structured CNFs@CAC with excellent water wettability and oxidation resistance. *Appl. Surf. Sci.* **2022**, *573*, 151497. DOI:10.1016/j.apsusc.2021.151497
30. Xiao G, Yang S, Ding D, Ren Y, Lv L, Yang P, et al. One-step synthesis of *in-situ* carbon-containing calcium aluminate cement as binders for refractory castables. *Ceram. Int.* **2018**, *44*, 15378–15384. DOI:10.1016/j.ceramint.2018.05.189
31. Han B, Wang P, Ke C, Yan W, Wei Y, Li N. Hydration behavior of spinel containing high alumina cement from high titania blast furnace slag. *Cem. Concr. Res.* **2016**, *79*, 257–264. DOI:10.1016/j.cemconres.2015.09.019
32. Holleyn F, Waldstädt T, Kasper J, Dannert C, Krause O. Effects of Changing the Specific Surface Area in the Ceramic Matrix of CAC-Containing Refractory Castables on the Initial Stiffening and Setting Behaviour. *High-Temp. Mater.* **2025**, *2*, 10009. DOI:10.70322/htm.2025.10009
33. Silva AP, Segadães AM, Pinto DG, Oliveira LA, Devezas TC. Effect of particle size distribution and calcium aluminate cement on the rheological behaviour of all-alumina refractory castables. *Powder Technol.* **2012**, *226*, 107–113. DOI:10.1016/j.powtec.2012.04.028
34. Currell BR, Grzeskowlak R, Mldgley HG, Parsonage JR. The acceleration and retardation of set high alumina cement by additives. *Cem. Concr. Res.* **1987**, *17*, 420–432. DOI:10.1016/0008-8846(87)90006-8
35. Barret PP, Ménétrier D, Bertrandie D. Contribution to the study of the kinetic mechanism of aluminous cement setting I—Latent periods in heterogeneous and homogeneous milieus and the absence of heterogeneous nucleation. *Cem. Concr. Res.* **1974**, *4*, 545–556. DOI:10.1016/0008-8846(74)90005-2
36. Barret P, Ménétrier D. Contribution to the study of the kinetic mechanism of aluminous cement setting II—Release of the factor resposible for breaking the latent period by the dissolution of a fraction of the initial cement. *Cem. Concr. Res.* **1974**, *4*, 723–733. DOI:10.1016/0008-8846(74)90044-1
37. Oliveira IR, Pandolfelli VC. Castable matrix, additives and their role on hydraulic binder hydration. *Ceram. Int.* **2009**, *35*, 1453–1460. DOI:10.1016/j.ceramint.2008.07.024